

# Band offsets at metalorganic chemical vapor deposited $\beta$ -(Al<sub>x</sub>Ga<sub>1-x</sub>)<sub>2</sub>O<sub>3</sub>/ $\beta$ -Ga<sub>2</sub>O<sub>3</sub> interfaces- Crystalline orientation dependence

A F M Anhar Uddin Bhuiyan<sup>1,a)</sup>, Zixuan Feng<sup>1</sup>, Hsien-Lien Huang<sup>2</sup>, Lingyu Meng<sup>1</sup>, Jinwoo Hwang<sup>2</sup>, and Hongping Zhao<sup>1,2,b)</sup>

<sup>1</sup>Department of Electrical and Computer Engineering, The Ohio State University, Columbus, OH 43210, USA

<sup>2</sup>Department of Materials Science and Engineering, The Ohio State University, Columbus, OH 43210, USA

<sup>a)</sup>Email: [bhuiyan.13@osu.edu](mailto:bhuiyan.13@osu.edu) <sup>b)</sup>Corresponding author Email: [zhao.2592@osu.edu](mailto:zhao.2592@osu.edu)

$\beta$ -(Al<sub>x</sub>Ga<sub>1-x</sub>)<sub>2</sub>O<sub>3</sub> alloy represents an emerging ultrawide bandgap semiconductor material for applications in high power electronics and deep ultraviolet optoelectronics. The recent demonstrations of orientation-dependent epitaxial growth of high quality  $\beta$ -(Al<sub>x</sub>Ga<sub>1-x</sub>)<sub>2</sub>O<sub>3</sub> films have unlocked the prospects for the development of ultra-high frequency  $\beta$ -(Al<sub>x</sub>Ga<sub>1-x</sub>)<sub>2</sub>O<sub>3</sub>/Ga<sub>2</sub>O<sub>3</sub> based transistors with high power tolerance. To control the electronic and optical properties of  $\beta$ -(Al<sub>x</sub>Ga<sub>1-x</sub>)<sub>2</sub>O<sub>3</sub>/Ga<sub>2</sub>O<sub>3</sub> heterostructure based devices, understanding of the band offsets between  $\beta$ -(Al<sub>x</sub>Ga<sub>1-x</sub>)<sub>2</sub>O<sub>3</sub> and  $\beta$ -Ga<sub>2</sub>O<sub>3</sub> is crucial. However, there have been no systematic experimental studies on the evolution of the band offsets between differently oriented  $\beta$ -(Al<sub>x</sub>Ga<sub>1-x</sub>)<sub>2</sub>O<sub>3</sub>/Ga<sub>2</sub>O<sub>3</sub> heterointerfaces as a function of Al compositions. This work presents the valance and conduction band offsets at (010) and ( $\bar{2}$ 01) oriented  $\beta$ -(Al<sub>x</sub>Ga<sub>1-x</sub>)<sub>2</sub>O<sub>3</sub>/Ga<sub>2</sub>O<sub>3</sub> interfaces by using X-ray photoelectron spectroscopy.  $\beta$ -(Al<sub>x</sub>Ga<sub>1-x</sub>)<sub>2</sub>O<sub>3</sub> films with  $x \leq 0.35$  and  $x \leq 0.48$  were grown by metalorganic chemical vapor deposition (MOCVD) on (010) and ( $\bar{2}$ 01) oriented  $\beta$ -Ga<sub>2</sub>O<sub>3</sub> substrates, respectively. The determined band offsets reveal the formation of type-II (staggered) band alignment at (010) oriented  $\beta$ -(Al<sub>x</sub>Ga<sub>1-x</sub>)<sub>2</sub>O<sub>3</sub>/Ga<sub>2</sub>O<sub>3</sub> and type-I (straddling) heterojunction between ( $\bar{2}$ 01)  $\beta$ -(Al<sub>x</sub>Ga<sub>1-x</sub>)<sub>2</sub>O<sub>3</sub> and  $\beta$ -Ga<sub>2</sub>O<sub>3</sub>. For both crystalline orientations, the valance and conduction band offsets are found to increase with increasing Al content with a much weaker variation in the valance band offsets as compared to the conduction band offsets. Among

different orientations investigated, such as (010),  $(\bar{2}01)$ , and (100), the largest conduction band offset occurs at  $\beta$ -(Al<sub>x</sub>Ga<sub>1-x</sub>)<sub>2</sub>O<sub>3</sub>/Ga<sub>2</sub>O<sub>3</sub> interface with (100) orientation, providing opportunities for excellent electron confinement with high-density two-dimensional electron gas (2DEG). Results from this study on the tunable and orientation dependent band offsets with the variation of the Al alloy fraction will provide guidance for the design of heterostructures in future  $\beta$ -(Al<sub>x</sub>Ga<sub>1-x</sub>)<sub>2</sub>O<sub>3</sub>/Ga<sub>2</sub>O<sub>3</sub> based devices.

**Keywords:** ultrawide-band-gap semiconductors, metalorganic chemical vapor deposition (MOCVD), band offsets, X-ray photoelectron spectroscopy,  $\beta$ -(Al<sub>x</sub>Ga<sub>1-x</sub>)<sub>2</sub>O<sub>3</sub>

## I. Introduction

The combination of a very large bandgap energy (4.87 eV) [1], predicted high critical field strength (6-8 MV/cm) [2], and the ability to control the n-type conductivity in a wide range [3-5] have enabled  $\beta$ -Ga<sub>2</sub>O<sub>3</sub> for the development of high-power electronic devices, with a predicted breakdown field more than three times larger than GaN or SiC devices [2]. Extension of the bandgap from 4.87 eV ( $\beta$ -Ga<sub>2</sub>O<sub>3</sub>) to 8.82 eV ( $\alpha$ -Al<sub>2</sub>O<sub>3</sub>) by alloying with Al can extend the device performance even further, with much higher critical field strength and power tolerance [1]. Owing to its extremely high breakdown field strength, which is predicted to be as high as 16 MV/cm with 80% of Al composition [6], (Al<sub>x</sub>Ga<sub>1-x</sub>)<sub>2</sub>O<sub>3</sub> is promising for high power device applications. Moreover, through device scaling, lateral  $\beta$ -(Al<sub>x</sub>Ga<sub>1-x</sub>)<sub>2</sub>O<sub>3</sub>/Ga<sub>2</sub>O<sub>3</sub> heterostructures based devices can also gain benefits of its large bandgap in applications such as integrated power electronics and radio-frequency electronics [7-11].

Previous success on demonstration of nitride-based high electron mobility transistors (HEMTs) [12] and arsenide-based modulation-doped field-effect transistors (MODFETs) [13] is

built up on the concept of two-dimensional electron gas (2DEG) as the active layer. This has motivated the development of  $\beta$ -(Al<sub>x</sub>Ga<sub>1-x</sub>)<sub>2</sub>O<sub>3</sub>/Ga<sub>2</sub>O<sub>3</sub> heterostructure-based lateral devices to enhance the carrier density with higher mobilities by realizing the modulation doping near to  $\beta$ -(Al<sub>x</sub>Ga<sub>1-x</sub>)<sub>2</sub>O<sub>3</sub>/Ga<sub>2</sub>O<sub>3</sub> interface. Recent studies on the modulation doping in  $\beta$ -(Al<sub>x</sub>Ga<sub>1-x</sub>)<sub>2</sub>O<sub>3</sub>/Ga<sub>2</sub>O<sub>3</sub> heterostructures have exhibited promising characteristics with decent carrier densities and mobilities [7-11]. Since the first proof-of-concept  $\beta$ -(Al<sub>x</sub>Ga<sub>1-x</sub>)<sub>2</sub>O<sub>3</sub>/Ga<sub>2</sub>O<sub>3</sub> based MODFET device demonstration [7, 14], significant efforts and progresses have been made for the development of  $\beta$ -(Al<sub>x</sub>Ga<sub>1-x</sub>)<sub>2</sub>O<sub>3</sub> epitaxy [15-24] and  $\beta$ -(Al<sub>x</sub>Ga<sub>1-x</sub>)<sub>2</sub>O<sub>3</sub>/Ga<sub>2</sub>O<sub>3</sub> heterostructure based devices [7-11]. Note that high-Al  $\beta$ -(Al<sub>x</sub>Ga<sub>1-x</sub>)<sub>2</sub>O<sub>3</sub>/Ga<sub>2</sub>O<sub>3</sub> hetero-interfaces with larger band offsets [1, 25] can facilitate to generate higher sheet charge density with higher mobilities [26]. Several studies on the epitaxial growth of  $\beta$ -(Al<sub>x</sub>Ga<sub>1-x</sub>)<sub>2</sub>O<sub>3</sub> thin films on differently oriented  $\beta$ -Ga<sub>2</sub>O<sub>3</sub> substrates such as (010) [15, 17-19], (100) [16, 20, 21] and ( $\bar{2}$ 01) [22] have been conducted by utilizing different growth methods, including metalorganic chemical vapor deposition (MOCVD) [18-22] and molecular beam epitaxy (MBE) [15-17]. While MOCVD grown  $\beta$ -(Al<sub>x</sub>Ga<sub>1-x</sub>)<sub>2</sub>O<sub>3</sub> films on (100) [20, 21] and ( $\bar{2}$ 01) [22]  $\beta$ -Ga<sub>2</sub>O<sub>3</sub> substrates exhibited higher Al incorporation above 50%, (010)  $\beta$ -(Al<sub>x</sub>Ga<sub>1-x</sub>)<sub>2</sub>O<sub>3</sub> films showed limited Al incorporation in the  $\beta$ -phase [18, 19, 27-29], indicating strong orientation dependence of  $\beta$ -(Al<sub>x</sub>Ga<sub>1-x</sub>)<sub>2</sub>O<sub>3</sub> epitaxy on top of  $\beta$ -Ga<sub>2</sub>O<sub>3</sub> substrates. Although there have been several efforts on the epitaxial growth of  $\beta$ -(Al<sub>x</sub>Ga<sub>1-x</sub>)<sub>2</sub>O<sub>3</sub> films in a wide composition range, the properties for 2DEG device design such as the evolution of the band offsets with increasing Al composition are not well reported experimentally, which is crucial for the design of  $\beta$ -(Al<sub>x</sub>Ga<sub>1-x</sub>)<sub>2</sub>O<sub>3</sub>/Ga<sub>2</sub>O<sub>3</sub> based device structures.

X-ray photoelectron spectroscopy (XPS) has been considered as a non-destructive method [30-32] to measure band offsets at heterointerfaces. By utilizing XPS, band alignments at insulating oxides such as SiO<sub>2</sub> [33] and  $\gamma$ -Al<sub>2</sub>O<sub>3</sub> [34] with  $\beta$ -Ga<sub>2</sub>O<sub>3</sub> interfaces were reported. The conduction and valence band offsets were determined to be  $1.5 \pm 0.2$  eV and  $0.7 \pm 0.2$  eV respectively, between the atomic layer deposited (ALD) Al<sub>2</sub>O<sub>3</sub> and  $\beta$ -Ga<sub>2</sub>O<sub>3</sub> interface by using XPS [35]. On the other hand, the conduction band offset of 1.7 eV at ALD deposited Al<sub>2</sub>O<sub>3</sub>/ $\beta$ -Ga<sub>2</sub>O<sub>3</sub> interfaces was measured by utilizing capacitance-voltage profiling method [36]. PLD grown  $\gamma$ -Al<sub>2</sub>O<sub>3</sub>/ $\beta$ -Ga<sub>2</sub>O<sub>3</sub> interfaces exhibited the conduction band offset of 1.9 eV and valence band offset of 0.5 eV [33], indicating a considerable deviation in the band offset values as compared to the ALD deposited Al<sub>2</sub>O<sub>3</sub>. Another study conducted by Carey IV et al. [37] determined the valence band offsets of  $0.07 \pm 0.20$  eV (straddling gap, type-I alignment) and  $-0.86 \pm 0.25$  eV (staggered gap, type-II alignment) at ALD and sputtered Al<sub>2</sub>O<sub>3</sub>/ $\bar{2}01$   $\beta$ -Ga<sub>2</sub>O<sub>3</sub> heterointerfaces, respectively. Moreover, there have been several studies on the band offset measurements of SiO<sub>2</sub> or HfO<sub>2</sub>/ $\beta$ -(Al<sub>x</sub>Ga<sub>1-x</sub>)<sub>2</sub>O<sub>3</sub> heterointerfaces, which showed a strong dependency of the valence band offsets on the Al compositions [38-41].

While there are quite a few reports on the band offset measurements of insulating oxides to  $\beta$ -Ga<sub>2</sub>O<sub>3</sub> or  $\beta$ -(Al<sub>x</sub>Ga<sub>1-x</sub>)<sub>2</sub>O<sub>3</sub> films, very few investigations have been carried out on the band offset measurements at  $\beta$ -(Al<sub>x</sub>Ga<sub>1-x</sub>)<sub>2</sub>O<sub>3</sub>/Ga<sub>2</sub>O<sub>3</sub> interfaces. By varying the Al compositions up to 52%, our recent study revealed the formation of type-II (staggered gap) band alignment at MOCVD grown (100)  $\beta$ -(Al<sub>x</sub>Ga<sub>1-x</sub>)<sub>2</sub>O<sub>3</sub>/Ga<sub>2</sub>O<sub>3</sub> interfaces with conduction and valence band offset of  $1.21 \pm 0.16$  eV and  $0.19 \pm 0.06$  eV ( $x = 0.52$ ), respectively [21]. Theoretical calculations based on density functional theory (DFT) predicted the increase of the valence and the conduction band offsets with increasing Al composition with type-II band alignment at (010)  $\beta$ -

$(\text{Al}_x\text{Ga}_{1-x})_2\text{O}_3/\text{Ga}_2\text{O}_3$  interfaces [1, 25]. Very recently, another theoretical work by Mu et al. on the orientation dependent band offsets between  $\beta\text{-(Al}_x\text{Ga}_{1-x})_2\text{O}_3$  and  $\beta\text{-Ga}_2\text{O}_3$  revealed the occurrence of the largest conduction band offsets for (100) oriented  $\beta\text{-(Al}_x\text{Ga}_{1-x})_2\text{O}_3/\text{Ga}_2\text{O}_3$  interfaces as compared to other orientations such as (010), (001), or  $(\bar{2}01)$  [42]. Although a distinct dependence of the band offsets between  $\beta\text{-(Al}_x\text{Ga}_{1-x})_2\text{O}_3$  and  $\beta\text{-Ga}_2\text{O}_3$  on the crystal orientations has been predicted by theoretical calculations [42], experimental measurements on the band offsets for differently oriented  $\beta\text{-(Al}_x\text{Ga}_{1-x})_2\text{O}_3/\text{Ga}_2\text{O}_3$  interfaces are still lacking.

In this work, the dependence of the valance and the conduction band offsets with the increase of the Al composition is studied for (010) and  $(\bar{2}01)$  oriented  $\beta\text{-(Al}_x\text{Ga}_{1-x})_2\text{O}_3/\text{Ga}_2\text{O}_3$  heterointerfaces. Phase pure  $\beta\text{-(Al}_x\text{Ga}_{1-x})_2\text{O}_3$  films in a wide composition range were grown on (010) ( $x \leq 0.35$ ) and  $(\bar{2}01)$  ( $x \leq 0.48$ )  $\beta\text{-Ga}_2\text{O}_3$  substrates. The surface morphology, crystalline structure and quality, the interface abruptness, and the strain in the films are investigated by comprehensive characterization techniques, including atomic force microscopy (AFM), x-ray diffraction (XRD), reciprocal space mapping (RSM), and scanning transmission electron microscopy (STEM). The bandgaps and the band offsets between  $\beta\text{-(Al}_x\text{Ga}_{1-x})_2\text{O}_3$  and  $\beta\text{-Ga}_2\text{O}_3$  heterointerfaces grown along different orientations with different Al compositions are determined by using XPS. While type-II band alignments are extracted at (010)  $\beta\text{-(Al}_x\text{Ga}_{1-x})_2\text{O}_3/\text{Ga}_2\text{O}_3$  interfaces, the  $(\bar{2}01)$  orientation exhibits type-I band alignments for all the Al compositions investigated. These results show a good agreement with theoretically predicted band offsets at  $\beta\text{-(Al}_x\text{Ga}_{1-x})_2\text{O}_3/\text{Ga}_2\text{O}_3$  interfaces along different orientations. Results from this study will provide guidance for  $\beta\text{-(Al}_x\text{Ga}_{1-x})_2\text{O}_3/\text{Ga}_2\text{O}_3$  heterostructure device design and modeling.

## II. Experimental details

### II A. Material growth via MOCVD

The investigated  $\beta$ -( $\text{Al}_x\text{Ga}_{1-x}$ ) $_2\text{O}_3$  thin films were grown on Fe doped semi-insulating (010) and Sn doped conductive ( $\bar{2}01$ )  $\beta$ - $\text{Ga}_2\text{O}_3$  substrates. The substrates were commercially acquired from Novel Crystal Technology, Inc. Triethylgallium (TEGa), Trimethylaluminum (TMAI), and pure  $\text{O}_2$  were used as Ga, Al, and O precursors, respectively. Argon (Ar) was used as the carrier gas. The chamber pressure for the growth of (010)  $\beta$ -( $\text{Al}_x\text{Ga}_{1-x}$ ) $_2\text{O}_3$  thin films was kept at 20 torr. However, the pressure was varied from 20 to 80 torr for the growth of ( $\bar{2}01$ )  $\beta$ -( $\text{Al}_x\text{Ga}_{1-x}$ ) $_2\text{O}_3$  films. The growth temperature was fixed at 880 °C for all the growths along different orientations. For tuning the Al composition of the alloy layers, [TMAI]/[TEGa+TMAI] molar flow rate ratio was varied from 2.35% to 18.08% with an  $\text{O}_2$  flow rate of 500 sccm. Prior to loading the substrates into the growth chamber, an ex-situ cleaning was performed by using solvents. To remove any potential contamination from the growth surface, all the substrates were treated with high temperature (920°C) in-situ annealing for 5 mins under  $\text{O}_2$  atmosphere. A detailed description of the MOCVD growth of (010) and ( $\bar{2}01$ ) oriented  $\beta$ -( $\text{Al}_x\text{Ga}_{1-x}$ ) $_2\text{O}_3$  thin films can be found in refs [18, 19] and [22], respectively.

### II B. Materials characterization methods

The growth of pure  $\beta$ -phase ( $\text{Al}_x\text{Ga}_{1-x}$ ) $_2\text{O}_3$  alloys was confirmed by high resolution XRD measurements, where a Bruker D8 Discover with Cu  $K_\alpha$  radiation as x-ray source (wavelength,  $\lambda = 1.5418\text{\AA}$ ) was used. In addition, the crystalline quality, structure, Al composition, and the strain of the films were also evaluated by XRD  $\omega$ -2 $\theta$  and RSM scans. The surface morphology and surface roughness were estimated via atomic force microscopy using a Bruker AXS

Dimension Icon. A Thermo Fisher Scientific Themis-Z scanning transmission electron microscope, operated at 200 kV ( $Cs_3=0.002$  mm,  $Cs_5=1.0$  mm) with probe convergence half angles of 17.9 mrad, was used to obtain high resolution high angle annular dark field (HAADF) STEM images. The Al compositions, band gaps, and the band offsets were determined by investigating the chemical bonding states of  $\beta\text{-Ga}_2\text{O}_3$  and  $\beta\text{-(Al}_x\text{Ga}_{1-x})_2\text{O}_3$  alloys with different Al compositions using XPS (Kratos Axis Ultra X-ray photoelectron spectrometer). A monochromic Al  $K\alpha$  x-ray source with a photon energy of 1486.6 eV was used for the measurement with an energy resolution of 0.1 eV. The charge neutralizer gun was used to eliminate the charging effect during the measurement. C 1s core level peak at 284.8 eV from the adventitious carbon on the sample was used as a reference to calibrate the binding energy.

### **II C. Sample preparation for XPS measurement**

Three types of samples were prepared for both (010) and  $(\bar{2}01)$  orientations to measure the band offsets at  $\beta\text{-(Al}_x\text{Ga}_{1-x})_2\text{O}_3/\text{Ga}_2\text{O}_3$  interfaces by using XPS, as shown in the schematics of Figure 1 : (i)  $\sim 150$  nm thick  $\beta\text{-Ga}_2\text{O}_3$  film grown on (010) and  $(\bar{2}01)$   $\beta\text{-Ga}_2\text{O}_3$  substrates; (ii)  $\sim 25$  nm thick  $\beta\text{-(Al}_x\text{Ga}_{1-x})_2\text{O}_3$  layer with Al composition  $x = 0.16, 0.26$  and  $0.35$  [(010) orientation] and  $x = 0.17$  and  $0.48$  [ $(\bar{2}01)$  orientation] grown on top of  $\sim 65$  nm thick (010) and  $(\bar{2}01)$   $\beta\text{-Ga}_2\text{O}_3$  layers, respectively; (iii) very thin ( $\sim 2$  nm) (010) and  $(\bar{2}01)$  oriented  $\beta\text{-(Al}_x\text{Ga}_{1-x})_2\text{O}_3$  layer grown on top of  $\sim 65$  nm  $\beta\text{-Ga}_2\text{O}_3$  layer on (010) and  $(\bar{2}01)$   $\beta\text{-Ga}_2\text{O}_3$  substrates to capture all the electronic states from the  $\beta\text{-(Al}_x\text{Ga}_{1-x})_2\text{O}_3/\text{Ga}_2\text{O}_3$  interfaces.

## **III. Results**

### **III A. Material characterization**

In order to evaluate the structural quality of the epi-films, high-resolution XRD was performed on both (010) and ( $\bar{2}01$ )  $\beta$ - $(\text{Al}_x\text{Ga}_{1-x})_2\text{O}_3$  films grown with different Al compositions. Figures S1 (a) and (b) in the Supplementary material show the XRD  $\omega$ - $2\theta$  spectra for  $\beta$ - $(\text{Al}_x\text{Ga}_{1-x})_2\text{O}_3$  films grown on (010) and ( $\bar{2}01$ )  $\beta$ - $\text{Ga}_2\text{O}_3$  substrates, respectively. Prominent diffraction peaks from (020) [for (010) orientation] and ( $\bar{6}03$ ) [for ( $\bar{2}01$ ) orientation] reflections of  $\beta$ - $(\text{Al}_x\text{Ga}_{1-x})_2\text{O}_3$  films for different Al compositions are observed without any phase segregation. The Al compositions of  $x = 0.16, 0.26$  and  $0.35$  [for (010) orientation] and  $x = 0.17$  and  $0.48$  [for ( $\bar{2}01$ ) orientation] are extracted by analyzing the distances between the peak positions of the substrate and the epilayers [18, 19, 22], which show good agreement with XPS results as discussed in a later section. High intensity diffraction peaks with rocking curve FWHMs of 47, 113 and 89 arcsec for  $x = 0.16, 0.26$  and  $0.35$  [(010)  $\beta$ - $(\text{Al}_x\text{Ga}_{1-x})_2\text{O}_3$  films] and 91 and 624 arcsec for  $x = 0.17$  and  $0.48$  [( $\bar{2}01$ )  $\beta$ - $(\text{Al}_x\text{Ga}_{1-x})_2\text{O}_3$  films] are measured, indicating the growth of phase pure  $\beta$ - $(\text{Al}_x\text{Ga}_{1-x})_2\text{O}_3$  films on both (010) and ( $\bar{2}01$ )  $\beta$ - $\text{Ga}_2\text{O}_3$  substrates.

The strain in the epitaxial  $\beta$ - $(\text{Al}_x\text{Ga}_{1-x})_2\text{O}_3$  films grown along both (010) and ( $\bar{2}01$ ) orientations are investigated by using asymmetrical reciprocal space maps (RSM), as exemplarily shown in Figures 2(a) and (b) for (420) reflection of (010) oriented  $\beta$ - $(\text{Al}_{0.35}\text{Ga}_{0.65})_2\text{O}_3$  and ( $\bar{4}03$ ) reflection of ( $\bar{2}01$ )  $\beta$ - $(\text{Al}_{0.48}\text{Ga}_{0.52})_2\text{O}_3$  films, respectively. The vertical and diagonal dashed line represents the fully strained and fully relaxed positions, respectively. Both (420)  $\beta$ - $(\text{Al}_x\text{Ga}_{1-x})_2\text{O}_3$  ( $x = 0.35$ ) and ( $\bar{4}03$ )  $\beta$ - $(\text{Al}_x\text{Ga}_{1-x})_2\text{O}_3$  ( $x = 0.48$ ) peaks are found to be slightly shifted towards the fully relaxed line, which indicates that the films may not be under fully in-plane tensile strain with Al compositions of 35% (010) and 48% ( $\bar{2}01$ ).

In addition, the surface roughness can also affect the characterization as XPS is a surface sensitive technique. To evaluate the surface feature and surface roughness of  $\beta$ -(Al<sub>x</sub>Ga<sub>1-x</sub>)<sub>2</sub>O<sub>3</sub> films, AFM imaging was performed. Figures 3 (a-d) and (e-f) show the surface AFM images for (010) and ( $\bar{2}01$ ) oriented  $\beta$ -Ga<sub>2</sub>O<sub>3</sub> and  $\beta$ -(Al<sub>x</sub>Ga<sub>1-x</sub>)<sub>2</sub>O<sub>3</sub> films with different Al compositions, respectively. The RMS roughness of (010) films ranges between 0.35 nm and 1.38 nm. However, due to the appearance of elongated granular surface morphology, the RMS roughness of ( $\bar{2}01$ ) oriented  $\beta$ -(Al<sub>x</sub>Ga<sub>1-x</sub>)<sub>2</sub>O<sub>3</sub> films ranging between 2.09 nm and 4.35 nm are found to be relatively higher than those of (010) orientations.

Moreover, the interface quality of  $\beta$ -(Al<sub>x</sub>Ga<sub>1-x</sub>)<sub>2</sub>O<sub>3</sub>/Ga<sub>2</sub>O<sub>3</sub> heterostructures is important for determining the band offsets. The interfacial abruptness at the  $\beta$ -(Al<sub>x</sub>Ga<sub>1-x</sub>)<sub>2</sub>O<sub>3</sub>/Ga<sub>2</sub>O<sub>3</sub> heterostructures grown along both (010) and ( $\bar{2}01$ ) orientations are investigated by atomic resolution STEM imaging. Figures 4 (a-c) and (d-e) show the cross-sectional HAADF-STEM images of  $\beta$ -(Al<sub>x</sub>Ga<sub>1-x</sub>)<sub>2</sub>O<sub>3</sub>/Ga<sub>2</sub>O<sub>3</sub> heterostructures grown on (010) [ $x = 0.16, 0.26$  and  $0.35$ ] and ( $\bar{2}01$ ) [ $x = 0.17$  and  $0.48$ ]  $\beta$ -Ga<sub>2</sub>O<sub>3</sub> substrates, respectively. The position of the interface was primarily determined by the contrast in the HAADF STEM images shown in Fig. 4. The column intensities of individual atomic columns are strongly dependent on the atomic number ( $Z$ ) of the constituent atomic species, and therefore they provide an intuitive understanding of the composition change at the interface. The dark and bright contrasts in Fig. 4 represent the  $\beta$ -(Al<sub>x</sub>Ga<sub>1-x</sub>)<sub>2</sub>O<sub>3</sub> and  $\beta$ -Ga<sub>2</sub>O<sub>3</sub> layers, respectively. All the samples grown with different Al compositions show abrupt interfaces as evidenced by the sharp contrast between  $\beta$ -(Al<sub>x</sub>Ga<sub>1-x</sub>)<sub>2</sub>O<sub>3</sub> and  $\beta$ -Ga<sub>2</sub>O<sub>3</sub> layers, indicating the growth of phase pure  $\beta$ -(Al<sub>x</sub>Ga<sub>1-x</sub>)<sub>2</sub>O<sub>3</sub> films with high quality  $\beta$ -(Al<sub>x</sub>Ga<sub>1-x</sub>)<sub>2</sub>O<sub>3</sub>/Ga<sub>2</sub>O<sub>3</sub> interfaces.

### III B. Elemental compositions determination by XPS

The elemental compositions of  $\beta\text{-(Al}_x\text{Ga}_{1-x})_2\text{O}_3$  films were determined by investigating the XPS core level spectra. Due to the large sampling depth, the reliable extraction of the elemental compositions of thin films by using energy dispersive x-ray spectroscopy (EDX) or Rutherford backscattering methods is difficult. XPS technique which has the sampling depth of only a few nanometers, is suitable for such measurement. The XPS survey spectra of  $\beta\text{-(Al}_x\text{Ga}_{1-x})_2\text{O}_3$  films with different Al compositions exhibited no metallic contaminants as shown in Figure S2 of the Supplementary material, indicating highly pure  $\beta\text{-(Al}_x\text{Ga}_{1-x})_2\text{O}_3$  alloys grown along both (010) and ( $\bar{2}$ 01) orientations. The determination of the Al compositions for both (010) and ( $\bar{2}$ 01) films were performed by using the areas of Ga 3s and Al 2p core level spectra after subtracting the Shirley background and using the relative sensitivity factors of Ga 3s ( $S_{\text{Ga } 3s} = 1.13$ ) and Al 2p ( $S_{\text{Al } 2p} = 0.5371$ ) as shown in Figure 5. The Al compositions in (010)  $\beta\text{-(Al}_x\text{Ga}_{1-x})_2\text{O}_3$  films were determined as 16%, 26%, and 35%. Similarly, Al contents of 17% and 48% were estimated for ( $\bar{2}$ 01)  $\beta\text{-(Al}_x\text{Ga}_{1-x})_2\text{O}_3$  films. The Al compositions were also confirmed by measuring the area of Ga 3s and Al 2s ( $S_{\text{Al } 2s} = 0.753$ ) core level spectra. The Al contents calculated by the XPS technique closely match with the Al compositions estimated by XRD measurements. The detailed calculations of all Al contents are summarized in Table S1 (a) and (b) of the Supplementary material.

### III C. Band gap determination

An accurate estimation of the conduction band offsets at a heterojunction requires the bandgap information of both constituent materials of the heterostructure. It has been well established that the inelastic energy loss spectra that appear as broadened copies of strong

intensity core level peaks at the higher binding energy side can provide the bandgap information of wide-band-gap semiconductor materials [20-22, 33-35, 37, 43]. This is because the energetically fundamental lower limit of the inelastic scattering that is experienced by a photoelectron during its journey from the bulk to the surface is the excitation from the valance band to the conduction band. That is why the onset of the inelastic loss spectra at the higher binding energy side of the core level peak corresponds to the bandgap energy [44]. In this work, the bandgaps of  $\beta$ -Ga<sub>2</sub>O<sub>3</sub> and  $\beta$ -(Al<sub>x</sub>Ga<sub>1-x</sub>)<sub>2</sub>O<sub>3</sub> films with different Al compositions were determined by using O 1s core level peak, as exemplarily illustrated in Figure 6 (a), for ( $\bar{2}01$ )  $\beta$ -(Al<sub>x</sub>Ga<sub>1-x</sub>)<sub>2</sub>O<sub>3</sub> films with 48% Al composition. The inset figure represents the zoomed view of the background region of the O 1s peak. The intersection of the linear fitting of the inelastic background to the constant background represents the energy of the onset of inelastic loss spectra. By determining the onset of inelastic loss relative to O 1s peak, the bandgap for ( $\bar{2}01$ )  $\beta$ -(Al<sub>0.48</sub>Ga<sub>0.52</sub>)<sub>2</sub>O<sub>3</sub> films are estimated to be  $5.79 \pm 0.12$  eV. All the bandgap energies determined by this method for  $\beta$ -Ga<sub>2</sub>O<sub>3</sub> and  $\beta$ -(Al<sub>x</sub>Ga<sub>1-x</sub>)<sub>2</sub>O<sub>3</sub> films with different Al compositions are summarized in Table 1 (a) and (b). The bandgap of  $\beta$ -Ga<sub>2</sub>O<sub>3</sub> and  $\beta$ -(Al<sub>x</sub>Ga<sub>1-x</sub>)<sub>2</sub>O<sub>3</sub> films grown along (010) and ( $\bar{2}01$ ) orientations with different Al compositions are plotted in Figure 6 (b). The bandgap energies for all the investigated samples are found to increase with increasing Al compositions, which show a good agreement with theoretically predicted bandgap values [1].

#### III D. Valance and conduction band offset determination

For the determination of valance band offsets, we employed Kraut's method [30] by analyzing the valance-band (VB) spectra of both  $\beta$ -Ga<sub>2</sub>O<sub>3</sub> and  $\beta$ -(Al<sub>x</sub>Ga<sub>1-x</sub>)<sub>2</sub>O<sub>3</sub> films, Ga 2p<sub>3/2</sub> core level of  $\beta$ -Ga<sub>2</sub>O<sub>3</sub> films, and Al 2p/Al 2s peak of  $\beta$ -(Al<sub>x</sub>Ga<sub>1-x</sub>)<sub>2</sub>O<sub>3</sub> films. By calculating the

difference between the valance band maximum (VBM) and core levels for two pristine materials, the valance band offsets in a heterostructure can be determined by using the core level binding energies of both materials. The employed energy levels for  $\beta$ -(Al<sub>x</sub>Ga<sub>1-x</sub>)<sub>2</sub>O<sub>3</sub>/Ga<sub>2</sub>O<sub>3</sub> heterointerfaces are shown schematically in Figure 7, with the parameters used for determining the valance ( $\Delta E_v$ ) and the conduction ( $\Delta E_c$ ) band offsets between  $\beta$ -Ga<sub>2</sub>O<sub>3</sub> and  $\beta$ -(Al<sub>x</sub>Ga<sub>1-x</sub>)<sub>2</sub>O<sub>3</sub> alloys. The directions of  $\Delta E_v$  and  $\Delta E_c$  are defined such that the values of  $\Delta E_v$  and  $\Delta E_c$  are positive for type-I band alignment of  $\beta$ -(Al<sub>x</sub>Ga<sub>1-x</sub>)<sub>2</sub>O<sub>3</sub>/Ga<sub>2</sub>O<sub>3</sub> heterointerfaces. The bandgaps of  $\beta$ -Ga<sub>2</sub>O<sub>3</sub> and  $\beta$ -(Al<sub>x</sub>Ga<sub>1-x</sub>)<sub>2</sub>O<sub>3</sub> alloys are represented as  $E_g^{\text{GaO}}$  and  $E_g^{\text{AlGaO}}$ , respectively. The conduction band minimum (CBM), valance band maximum (VBM), and Ga 2p<sub>3/2</sub> core level for  $\beta$ -Ga<sub>2</sub>O<sub>3</sub> are defined as  $E_{\text{CBM}}^{\text{GaO}}$ ,  $E_{\text{VBM}}^{\text{GaO}}$ , and  $E_{\text{Ga } 2p_{3/2}}^{\text{GaO}}$ , respectively. Similarly, for  $\beta$ -(Al<sub>x</sub>Ga<sub>1-x</sub>)<sub>2</sub>O<sub>3</sub> alloys, CBM, VBM and Al 2p core level are defined as  $E_{\text{CBM}}^{\text{AlGaO}}$ ,  $E_{\text{VBM}}^{\text{AlGaO}}$ , and  $E_{\text{Al } 2p}^{\text{AlGaO}}$ , respectively.

Using Figure 7, the following equations can be derived for  $\Delta E_v$  and  $\Delta E_c$  calculations:

$$\Delta E_v = (E_{\text{Ga } 2p_{3/2}}^{\text{GaO}} - E_{\text{VBM}}^{\text{GaO}}) - (E_{\text{Al } 2p}^{\text{AlGaO}} - E_{\text{VBM}}^{\text{AlGaO}}) - \Delta E_{\text{CL}} \quad (1)$$

$$\Delta E_c = E_g^{\text{AlGaO}} - E_g^{\text{GaO}} - \Delta E_v \quad (2)$$

Here,  $\Delta E_{\text{CL}} = (E_{\text{Ga } 2p_{3/2}}^{\text{GaO}} - E_{\text{Al } 2p}^{\text{AlGaO}})$  is the difference between the binding energies of Ga 2p<sub>3/2</sub> and Al 2p core levels measured from ~2nm thick  $\beta$ -(Al<sub>x</sub>Ga<sub>1-x</sub>)<sub>2</sub>O<sub>3</sub>/Ga<sub>2</sub>O<sub>3</sub> heterointerfaces as schematically shown in Figure 1(iii). Ga 2p<sub>3/2</sub> and Al 2p core levels and VB spectra of  $\beta$ -Ga<sub>2</sub>O<sub>3</sub> and  $\beta$ -(Al<sub>x</sub>Ga<sub>1-x</sub>)<sub>2</sub>O<sub>3</sub> films are shown exemplarily for 35% Al composition samples grown along (010) orientation in Figure 8. The Ga 2p<sub>3/2</sub> and Al 2p core level peak positions are determined by fitting with Voigt (mixed Lorentzian-Gaussian) line shapes after applying Shirley background subtraction. The VB onsets are determined from the intersection of the two lines estimated from

linear extrapolation of the leading edge of the VB spectra to the background. The advantage of this method for the determination of valence band offset is that it only considers the energy difference, not the absolute energy positions. Therefore, any shift in the XPS core level spectra, for example, due to the surface band banding effect as a result of the presence of surface states, may not affect the calculated valence band offset values. By utilizing equation (1), the valence band offsets up to  $-0.13 \pm 0.06$  eV [(010)  $\beta$ -(Al<sub>0.35</sub>Ga<sub>0.65</sub>)<sub>2</sub>O<sub>3</sub>] and  $0.20 \pm 0.06$  eV [ $\bar{2}01$ )  $\beta$ -(Al<sub>0.48</sub>Ga<sub>0.52</sub>)<sub>2</sub>O<sub>3</sub>] are determined from the fitted core levels and VB spectra. By using the valence band offsets and bandgap energies of  $\beta$ -Ga<sub>2</sub>O<sub>3</sub> and  $\beta$ -(Al<sub>x</sub>Ga<sub>1-x</sub>)<sub>2</sub>O<sub>3</sub> films, the conduction band offsets are calculated by employing equation (2). As compared to the valence band offsets, higher conduction band offsets up to  $0.57 \pm 0.20$  eV [(010)  $\beta$ -(Al<sub>0.35</sub>Ga<sub>0.65</sub>)<sub>2</sub>O<sub>3</sub>] and  $0.76 \pm 0.20$  eV [ $\bar{2}01$ )  $\beta$ -(Al<sub>0.48</sub>Ga<sub>0.52</sub>)<sub>2</sub>O<sub>3</sub>] are estimated by using the valence band offsets and the bandgaps of  $\beta$ -Ga<sub>2</sub>O<sub>3</sub> and  $\beta$ -(Al<sub>x</sub>Ga<sub>1-x</sub>)<sub>2</sub>O<sub>3</sub> films. Further verification of the valence and the conduction band offsets was also carried out by using Al 2s core level peak, which showed consistent  $\Delta E_v$  and  $\Delta E_c$  values with those obtained from Al 2p core levels. The core level binding energies and valence band onsets with calculated valence band and conduction band offsets for different Al compositions are summarized in Table 1(a) [for (010) orientation] and (b) [for  $\bar{2}01$ ) orientation].

#### IV. Discussions

The band alignments between  $\beta$ -(Al<sub>x</sub>Ga<sub>1-x</sub>)<sub>2</sub>O<sub>3</sub>/Ga<sub>2</sub>O<sub>3</sub> heterointerfaces grown along (010) and  $\bar{2}01$ ) orientations with Al compositions  $x = 0, 0.16, 0.26$  and  $0.35$  [for (010) orientation] and  $x = 0, 0.17$  and  $0.48$  [for  $\bar{2}01$ ) orientation] are plotted in Figures 9 (a) and (b) respectively. While all the investigated (010) oriented  $\beta$ -(Al<sub>x</sub>Ga<sub>1-x</sub>)<sub>2</sub>O<sub>3</sub>/Ga<sub>2</sub>O<sub>3</sub> interfaces with different Al compositions showed type-II (staggered) band alignment, the  $\bar{2}01$ ) orientations exhibited type-I

(straddling) band alignment between  $\beta\text{-(Al}_x\text{Ga}_{1-x})_2\text{O}_3$  and  $\beta\text{-Ga}_2\text{O}_3$  for both 17% and 48% Al compositions, which are consistent with theoretical predictions [42]. Previously, type-II band alignment between ALD deposited  $\text{Al}_2\text{O}_3/(\bar{2}01)$   $\beta\text{-Ga}_2\text{O}_3$  heterointerface was reported [37], which is in good agreement with our finding for  $(\bar{2}01)$  orientation. Although the valance and conduction band offsets increase with increasing Al compositions, much smaller variations in the valance band offsets with the variation of Al compositions are noticed as compared to those of the conduction band offsets. Such smaller variations in the valance band offsets were also observed from previous experiments [21, 45] and are also predicted by theoretical DFT calculations [1, 25]. Compared to the valance band offsets of GaAs/AlAs [46, 47] and GaN/AlN [31, 48] heterojunctions, the valance band offsets  $\Delta E_v$  at  $\beta\text{-(Al}_x\text{Ga}_{1-x})_2\text{O}_3/\text{Ga}_2\text{O}_3$  heterointerfaces are found to be very small, as the top of the valance band is dominated by the localized O 2p states [1, 25, 49].

The comparison between the conduction band offsets ( $\Delta E_c$ ) at  $\beta\text{-(Al}_x\text{Ga}_{1-x})_2\text{O}_3/\text{Ga}_2\text{O}_3$  heterointerfaces grown along different orientations such as (010) and  $(\bar{2}01)$  are plotted in Figure 10. The  $\Delta E_c$  values determined in our previous study [21] for (100) oriented  $\beta\text{-(Al}_x\text{Ga}_{1-x})_2\text{O}_3/\text{Ga}_2\text{O}_3$  interfaces as a function of Al compositions are also included in the figure for comparison. The conduction band offsets exhibit strong orientation dependence as evidenced by the different  $\Delta E_c$  curves obtained for different orientations. For all orientations, the conduction band offsets increase with the increase of Al compositions. The bowing parameters of 1.25 eV (100) [21], 0.75 eV (010) and 0.80 eV  $(\bar{2}01)$  are determined from the quadratic fitting of  $\Delta E_c$  values. Among all the orientations investigated, (100) orientation shows the highest conduction band offsets, which is consistent with theoretical predictions [42].

Figure S3 in the Supplementary material shows the comparison between the experimental and theoretical conduction band offsets for (010), ( $\bar{2}01$ ), and (100)  $\beta$ -(Al<sub>x</sub>Ga<sub>1-x</sub>)<sub>2</sub>O<sub>3</sub>/Ga<sub>2</sub>O<sub>3</sub> heterointerfaces. The figure exhibits slightly higher experimental  $\Delta E_c$  values as compared to theoretical predictions for all three orientations. A recent theoretical study on the critical thicknesses for different orientations of  $\beta$ -(Al<sub>x</sub>Ga<sub>1-x</sub>)<sub>2</sub>O<sub>3</sub> films revealed that the (100) orientations can have the highest critical thickness as compared to other orientations such as (010), ( $\bar{2}01$ ), and (001) [50], which indicates that the strain in  $\beta$ -(Al<sub>x</sub>Ga<sub>1-x</sub>)<sub>2</sub>O<sub>3</sub> films grown on differently oriented  $\beta$ -Ga<sub>2</sub>O<sub>3</sub> substrates can be quite different. Moreover, the critical thicknesses of  $\beta$ -(Al<sub>x</sub>Ga<sub>1-x</sub>)<sub>2</sub>O<sub>3</sub> films were also predicted to reduce with increasing Al compositions [50]. Another study revealed that the conduction band offset at strained and unstrained  $\beta$ -Ga<sub>2</sub>O<sub>3</sub>/ $\theta$ -Al<sub>2</sub>O<sub>3</sub> interfaces can be different as the position of monoclinic  $\theta$ -Al<sub>2</sub>O<sub>3</sub> can be shifted to lower energy due to the effect of the strain in the films [42]. In this work, with around ~25 nm film thicknesses,  $\beta$ -(Al<sub>x</sub>Ga<sub>1-x</sub>)<sub>2</sub>O<sub>3</sub> films with different Al compositions grown on (010) and ( $\bar{2}01$ )  $\beta$ -Ga<sub>2</sub>O<sub>3</sub> substrates may not be fully strained (partial relaxation), which can cause slight deviations in the experimental results from the theoretical predictions that are calculated based on the assumptions of fully relaxed/strained conditions [42].

## V. Conclusion

In summary, experimental investigation of the band gaps and band offsets of (010) and ( $\bar{2}01$ ) oriented  $\beta$ -(Al<sub>x</sub>Ga<sub>1-x</sub>)<sub>2</sub>O<sub>3</sub>/Ga<sub>2</sub>O<sub>3</sub> with Al composition up to  $x \leq 0.35$  (010) and  $x \leq 0.48$  ( $\bar{2}01$ ) are performed. The bandgaps, estimated by analyzing the onset of the inelastic loss spectra, show an increasing trend with increasing Al contents for all the orientations investigated,

which are in a good agreement with theoretical predictions. XPS characterization reveals type-II band alignment at (010)  $\beta$ -(Al<sub>x</sub>Ga<sub>1-x</sub>)<sub>2</sub>O<sub>3</sub>/Ga<sub>2</sub>O<sub>3</sub> heterointerfaces, but type-I alignment for ( $\bar{2}01$ ) orientation for all Al compositions investigated. The determined valance band offset values show a slight increase with increasing Al compositions as compared to the conduction band offsets. The conduction band offsets up to  $0.57 \pm 0.20$  eV [ $x = 0.35$ , (010)] and  $0.76 \pm 0.20$  eV [ $x = 0.48$ , ( $\bar{2}01$ )] are determined, indicating the opportunity for strong electron confinement at  $\beta$ -(Al<sub>x</sub>Ga<sub>1-x</sub>)<sub>2</sub>O<sub>3</sub>/Ga<sub>2</sub>O<sub>3</sub> interfaces. The bowing parameters extracted from the quadratic fitting of the conduction band offsets are determined to be 0.75 eV and 0.80 eV for (010) and ( $\bar{2}01$ ) orientations, respectively. The (100) orientation showed the highest conduction band offsets as compared to those of (010) and ( $\bar{2}01$ ). These orientation-dependent band offset results will contribute to a better understanding of the electrical and optical properties of  $\beta$ -(Al<sub>x</sub>Ga<sub>1-x</sub>)<sub>2</sub>O<sub>3</sub> alloys as well as to help design  $\beta$ -(Al<sub>x</sub>Ga<sub>1-x</sub>)<sub>2</sub>O<sub>3</sub>/Ga<sub>2</sub>O<sub>3</sub> heterostructure devices and modeling.

See supplementary material at [URL will be inserted by AIP Publishing] for the XRD  $\omega$ -2 $\theta$  scans for (010) and ( $\bar{2}01$ )  $\beta$ -(Al<sub>x</sub>Ga<sub>1-x</sub>)<sub>2</sub>O<sub>3</sub> alloy with different Al compositions, XPS survey spectra, summary of Al compositions determined by using Ga 3s and Al 2s/Al 2p core level spectra, and the comparison between the experimental and theoretical band offsets.

## **Acknowledgements**

The authors acknowledge the Air Force Office of Scientific Research FA9550-18-1-0479 (AFOSR, Dr. Ali Sayir) for financial support. The authors also acknowledge the National Science Foundation (Grant No. 1810041, No. 2019753) and Semiconductor Research Corporation (SRC) under the Task ID GRC 3007.001 for partial support. Electron microscopy

was performed at the Center for Electron Microscopy and Analysis (CEMAS) at The Ohio State University.

### Data Availability Statements

The data that support the findings of this study are available from the corresponding author upon reasonable request.

### References

1. H. Peelaers, J. B. Varley, J. S. Speck, and C. G. Van de Walle, *Appl. Phys. Lett.* 112, 242101 (2018).
2. M. Higashiwaki, K. Sasaki, A. Kuramata, T. Masui, and S. Yamakoshi, *Appl. Phys. Lett.* 100, 013504 (2012).
3. Z. Feng, A. F. M. A. U. Bhuiyan, M. R. Karim, and H. Zhao, *Appl. Phys. Lett.* 114, 250601 (2019).
4. G. Seryogin, F. Alema, N. Valente, H. Fu, E. Steinbrunner, A. T. Neal, S. Mou, A. Fine, and A. Osinsky, *Appl. Phys. Lett.* 117, 262101 (2020).
5. Z. Feng, A. F. M. A. U. Bhuiyan, Z. Xia, W. Moore, Z. Chen, J. F. McGlone, D. R. Daughton, A. R. Arehart, S. A. Ringel, S. Rajan, and H. Zhao, *Phys. Status Solidi RPL*. 14, 2000145 (2020).
6. J. B. Varley, A. Perron, V. Lordi, D. Wickramaratne, and J. L. Lyons, *Appl. Phys. Lett.* 116, 172104 (2020).
7. S. Krishnamoorthy, Z. Xia, C. Joishi, Y. Zhang, J. McGlone, J. Johnson, M. Brenner, A. R. Arehart, J. Hwang, S. Lodha, and S. Rajan, *Appl. Phys. Lett.* 111, 023502 (2017).
8. Y. Zhang, A. Neal, Z. Xia, C. Joishi, J. M. Johnson, Y. Zheng, S. Bajaj, M. Brenner, D. Dorsey, K. Chabak, G. Jessen, J. Hwang, S. Mou, J. P. Heremans, and S. Rajan, *Appl. Phys. Lett.* 112, 173502 (2018).
9. N. K. Kalarickal, Z. Feng, A. F. M. A. U. Bhuiyan, Z. Xia, J. F. McGlone, W. Moore, A. R. Arehart, S. A. Ringel, H. Zhao, and S. Rajan, *IEEE Transaction on Electron Devices*, 68, 29-35 (2021).
10. P. Ranga, A. Bhattacharyya, A. Rishinaramangalam, Y. K Ooi, M. A. Scarpulla, D. Feezell and S. Krishnamoorthy, *Appl. Phys. Express* 13, 045501 (2020).
11. P. Ranga, A. Bhattacharyya, A. Chmielewski, S. Roy, R. Sun, M. A Scarpulla, N. Alem, and S. Krishnamoorthy, *Appl. Phys. Express* 14, 025501 (2021).

12. M. Micovic, N. Nguven, P. Janke, W. Wong, P. Hashimoto, L. McCray, and C. Nguyen, *Electron. Lett.* 36, 358 (2000).
13. P. M. Solomon and H. Mork, *IEEE Trans. Electron Devices* ED-31, 1015 (1984).
14. T. Oshima, Y. Kato, N. Kawano, A. Kuramata, S. Yamakoshi, S. Fujita, T. Oishi, and M. Kasu, *Appl. Phys. Express* 10(3), 035701 (2017).
15. S. W. Kaun, F. Wu, and J. S. Speck, *J. Vac. Sci. Technol. A* 33, 041508 (2015).
16. T. Oshima, T. Okuno, N. Arai, Y. Kobayashi, and S. Fujita, *Jpn. J. Appl. Phys. Part 1* 48, 070202 (2009).
17. P. Vogt, A. Mauze, F. Wu, B. Bonaf, and J. S. Speck, *Appl. Phys. Express* 11, 115503 (2018).
18. A F M A. U. Bhuiyan, Z. Feng, J. M. Johnson, Z. Chen, H.-L. Huang, J. Hwang, and H. Zhao, *Appl. Phys. Lett.* 115, 120602 (2019).
19. A F M A. U. Bhuiyan, Z. Feng, J. M. Johnson, H.-L. Huang, J. Sarker, M. Zhu, M. R. Karim, B. Mazumder, J. Hwang, and H. Zhao, *APL Mater.* 8, 031104 (2020).
20. A F M A. U. Bhuiyan, Z. Feng, J. M. Johnson, H.-L. Huang, J. Hwang, and H. Zhao, *Cryst. Growth Des.* 20, 6722 (2020).
21. A F M A. U. Bhuiyan, Z. Feng, J. M. Johnson, H.-L. Huang, J. Hwang, and H. Zhao, *Appl. Phys. Lett.* 117, 252105 (2020).
22. A F M A. U. Bhuiyan, Z. Feng, J. M. Johnson, H.-L. Huang, J. Hwang, and H. Zhao, *Appl. Phys. Lett.* 117, 142107 (2020).
23. H. Ghadi, J. F. McGlone, C. M Jackson, E. Farzana, Z. Feng, A. F. M. A. U. Bhuiyan, H. Zhao, A. R Arehart, S. A. Ringel, *APL Materials* 8, 021111 (2020).
24. H. Ghadi, J. F. McGlone, Z. Feng, A. F. M. A. U. Bhuiyan, H. Zhao, A. R. Arehart, S. A. Ringel, *Appl. Phys. Lett.* 117, 172106 (2020).
25. T. Wang, W. Li, C. Ni, and A. Janotti, *Phys. Rev. Appl.* 10, 011003 (2018).
26. K. Ghosh and U. Singiseti, *J. Mater. Res.* 32, 4142 (2017).
27. J. M. Johnson, H.-L. Huang, M. Wang, S. Mu, J. B. Varley, A. F. M. A. U. Bhuiyan, Z. Feng, N. K. Kalarickal, S. Rajan, H. Zhao, C. G. Van de Walle, and J. Hwang, *APL Materials* 9, 051103 (2021).
28. A F M A. U. Bhuiyan, Z. Feng, J. M. Johnson, H.-L. Huang, J. Sarker, M. Zhu, M. R. Karim, B. Mazumder, J. Hwang, and H. Zhao, *APL Materials* 8 (8), 089102 (2020).
29. J. Sarker, S. Broderick, A. F. M. A. U. Bhuiyan, Z. Feng, H. Zhao, and B. Mazumder, *Appl. Phys. Lett.* 116, 152101 (2020).
30. E. A. Kraut, R. W. Grant, J. R. Waldrop, and S. P. Kowalczyk, *Phys. Rev. Lett.* 44, 1620 (1980).
31. G. Martin, S. Strite, A. Botchkarev, A. Agarwal, A. Rockett, H. Morkoc, W. R. L. Lambrecht, and B. Segall, *Appl. Phys. Lett.* 65, 610 (1994).
32. X. Xua, X. Liub, Y. Guo, J. Wang, H. Song, S. Yang, H. Wei, Q. Zhuc, and Z. Wang, *J. Appl. Phys.* 107, 104510 (2010).
33. K. Konishi, T. Kamimura, M. H. Wong, K. Sasaki, A. Kuramata, S. Yamakoshi, and M. Higashiwaki, *Phys. Status Solidi* 253, 623 (2016).

34. M. Hattori, T. Oshima, R. Wakabayashi, K. Yoshimatsu, K. Sasaki, T. Masui, A. Kuramata, S. Yamakoshi, K. Horiba, H. Kumigashira, and A. Ohtomo, *Jpn. J. Appl. Phys., Part 1* 55, 1202B6 (2016).
35. T. Kamimura, K. Sasaki, M. H. Wong, D. Krishnamurthy, A. Kuramata, T. Masui, S. Yamakoshi, and M. Higashiwaki, *Appl. Phys. Lett.* 104, 192104 (2014).
36. T.-H. Hung, K. Sasaki, A. Kuramata, D. N. Nath, P. S. Park, C. Polchinski, and S. Rajan, *Appl. Phys. Lett.* 104, 162106 (2014).
37. P. H. Carey IV, F. Ren, D. C. Hays, B. P. Gila, S. J. Pearton, S. Jang, and A. Kuramata, *Vacuum* 142, 52 (2017).
38. C. Fares, F. Ren, E. Lambers, D. C. Hays, B. P. Gila, and S. J. Pearton, *J. Electron. Mater.* 48, 1568 (2019).
39. Z. Feng, Q. Feng, J. Zhang, X. Li, F. Li, L. Huang, H.-Y. Chen, H.-L. Lu, and Y. Hao, *Appl. Surf. Sci.* 434, 440 (2018).
40. C. Fares, M. Kneiß, H. von Wenckstern, M. Tadjer, F. Ren, E. Lambers, M. Grundmann, and S. J. Pearton, *ECS J. Solid State Sci. Technol.* 8, P351 (2019).
41. Z. Feng, Q. Feng, J. Zhang, C. Zhang, H. Zhou, X. Li, L. Huang, L. Xu, Y. Hu, S. Zhao, and Y. Hao, *J. Alloys Compd.* 745, 292 (2018).
42. S. Mu, H. Peelaers, Y. Zhang, M. Wang, and C. G. Van de Walle, *Appl. Phys. Lett.* 117, 252104 (2020).
43. T. Schultz, M. Kneiß, P. Storm, D. Splith, H. von Wenckstern, M. Grundmann, and N. Koch, *ACS Appl. Mater. Interfaces* 12, 8879 (2020).
44. M. T. Nichols, W. Li, D. Pei, G. A. Antonelli, Q. Lin, S. Banna, Y. Nishi, and J. L. Shohet, *J. Appl. Phys.* 115, 094105 (2014).
45. T. Uchida, R. Jinno, S. Takemoto, K. Kaneko, and S. Fujita, *Jpn. J. Appl. Phys.* 57, 040314 (2018).
46. S. B. Zhang, M. L. Cohen, S. G. Louie, D. Tomanek, and M. S. Hybersen, *Phys. Rev. B* 41, 10058 (1990).
47. A. Ichii, Y. Tsou, and E. Garmire, *J. Appl. Phys.* 74, 2112 (1993).
48. J. R. Waldrop and R. W. Grant, *Appl. Phys. Lett.* 68, 2879 (1996).
49. K. Yamaguchi, *Solid State Commun.* 131, 739 (2004).
50. S. Mu, M. Wang, H. Peelaers, and C. G. Van de Walle, *APL Mater.* 8, 091105 (2020).

**Table 1.** List of (a) (010) and (b) ( $\bar{2}01$ )  $\beta$ -( $\text{Al}_x\text{Ga}_{1-x}$ ) $_2\text{O}_3/\beta$ - $\text{Ga}_2\text{O}_3$  samples with different Al compositions. The corresponding bandgaps, valance and conduction band offsets determined by using the valance band spectra, Ga 2p $_{3/2}$ , Al 2p/Al 2s core levels are listed. The errors in the measured values are defined as the root-mean-square errors.

**(a) (010)  $\beta$ -( $\text{Al}_x\text{Ga}_{1-x}$ ) $_2\text{O}_3/\beta$ - $\text{Ga}_2\text{O}_3$**

Al composition	Bandgap (eV)	Core levels (CL)	$E_{\text{CL}}^{\text{GaO}}(\text{GaO})$	$E_{\text{CL}}^{\text{AlGaO}}(\text{AlGaO})$	$E_{\text{CL}}^{\text{AlGaO/GaO}}(\text{GaO})$	Valance band offset $\Delta E_v$ (eV)	Conduction band offset $\Delta E_c$ (eV)
			- $E_{\text{VBM}}^{\text{GaO}}$ (eV)	- $E_{\text{VBM}}^{\text{AlGaO}}$ (eV)	- $E_{\text{CL}}^{\text{AlGaO/GaO}}(\text{AlGaO})$ (eV)		
0%	$4.84 \pm 0.15$	Ga 2p $_{3/2}$	1114.72 $\pm 0.04$				
16%	$5.03 \pm 0.15$	Al 2p		70.86 $\pm 0.04$	1043.85 $\pm 0.02$	-0.001 $\pm 0.06$	0.19 $\pm 0.22$
		Al 2s		115.64 $\pm 0.04$	999.12 $\pm 0.02$	-0.04 $\pm 0.06$	0.23 $\pm 0.22$
26%	$5.18 \pm 0.12$	Al 2p		70.95 $\pm 0.04$	1043.87 $\pm 0.02$	-0.10 $\pm 0.06$	0.44 $\pm 0.20$
		Al 2s		115.76 $\pm 0.04$	999.03 $\pm 0.02$	-0.08 $\pm 0.06$	0.42 $\pm 0.20$
35%	$5.28 \pm 0.12$	Al 2p		71.01 $\pm 0.04$	1043.82 $\pm 0.02$	-0.11 $\pm 0.06$	0.55 $\pm 0.20$
		Al 2s		115.78 $\pm 0.04$	999.07 $\pm 0.02$	-0.13 $\pm 0.06$	0.57 $\pm 0.20$

**(b) ( $\bar{2}01$ )  $\beta$ -( $\text{Al}_x\text{Ga}_{1-x}$ ) $_2\text{O}_3/\beta$ - $\text{Ga}_2\text{O}_3$**

Al composition	Bandgap (eV)	Core levels (CL)	$E_{\text{CL}}^{\text{GaO}}(\text{GaO})$	$E_{\text{CL}}^{\text{AlGaO}}(\text{AlGaO})$	$E_{\text{CL}}^{\text{AlGaO/GaO}}(\text{GaO})$	Valance band offset $\Delta E_v$ (eV)	Conduction band offset $\Delta E_c$ (eV)
			- $E_{\text{VBM}}^{\text{GaO}}$ (eV)	- $E_{\text{VBM}}^{\text{AlGaO}}$ (eV)	- $E_{\text{CL}}^{\text{AlGaO/GaO}}(\text{AlGaO})$ (eV)		
0%	$4.85 \pm 0.15$	Ga 2p $_{3/2}$	1114.62 $\pm 0.04$				
17%	$5.17 \pm 0.16$	Al 2p		71.06 $\pm 0.04$	1043.43 $\pm 0.02$	0.13 $\pm 0.06$	0.19 $\pm 0.23$
		Al 2s		115.78 $\pm 0.04$	998.73 $\pm 0.02$	0.10 $\pm 0.06$	0.22 $\pm 0.23$
48%	$5.79 \pm 0.12$	Al 2p		71.23 $\pm 0.04$	1043.19 $\pm 0.02$	0.20 $\pm 0.06$	0.74 $\pm 0.20$
		Al 2s		116.02 $\pm 0.04$	998.41 $\pm 0.02$	0.18 $\pm 0.06$	0.76 $\pm 0.20$

## Figure Captions

**Figure 1** Samples prepared for the band offset measurements at  $\beta$ -( $\text{Al}_x\text{Ga}_{1-x}$ ) $_2\text{O}_3$ / $\beta$ - $\text{Ga}_2\text{O}_3$  interfaces: (i)  $\sim 150$  nm  $\beta$ - $\text{Ga}_2\text{O}_3$ , (ii)  $\sim 25$  nm thick  $\beta$ -( $\text{Al}_x\text{Ga}_{1-x}$ ) $_2\text{O}_3$ , (iii)  $\sim 2$  nm thick  $\beta$ -( $\text{Al}_x\text{Ga}_{1-x}$ ) $_2\text{O}_3$  layers grown on (010) and ( $\bar{2}01$ )  $\beta$ - $\text{Ga}_2\text{O}_3$  substrates. Al compositions in  $\beta$ -( $\text{Al}_x\text{Ga}_{1-x}$ ) $_2\text{O}_3$  layers are varied with  $x = 0.16, 0.26$  and  $0.35$  for (010) orientation and  $x = 0.17$  and  $0.48$  for ( $\bar{2}01$ ) orientation.

**Figure 2** Asymmetrical reciprocal space maps (RSM) around (a) (420) reflections of (010)  $\beta$ -( $\text{Al}_x\text{Ga}_{1-x}$ ) $_2\text{O}_3$  films with  $x = 35\%$  and (b) ( $\bar{4}03$ ) reflections of ( $\bar{2}01$ )  $\beta$ -( $\text{Al}_x\text{Ga}_{1-x}$ ) $_2\text{O}_3$  films with  $x = 48\%$  [sample structure (ii)]. Vertical and diagonal black dashed line represent fully strained and fully relaxed positions, respectively.

**Figure 3** Surface AFM images of (010) (a)  $\beta$ - $\text{Ga}_2\text{O}_3$  [sample structure (i)] and  $\beta$ -( $\text{Al}_x\text{Ga}_{1-x}$ ) $_2\text{O}_3$  films [sample structure (ii)] with Al compositions of (b)  $x = 16\%$ , (c)  $x = 26\%$ , and (d)  $x = 35\%$ . AFM images of ( $\bar{2}01$ ) oriented (e)  $\beta$ - $\text{Ga}_2\text{O}_3$  [sample structure (i)] film and  $\beta$ -( $\text{Al}_x\text{Ga}_{1-x}$ ) $_2\text{O}_3$  layer [sample structure (ii)] with Al compositions (f)  $x = 17\%$ , and (g)  $x = 48\%$  are also included.

**Figure 4** Atomic resolution cross-sectional HAADF-STEM images of  $\beta$ -( $\text{Al}_x\text{Ga}_{1-x}$ ) $_2\text{O}_3$ / $\beta$ - $\text{Ga}_2\text{O}_3$  interfaces, represented by white-dashed line, with Al compositions of (a)  $x = 16\%$ , (b)  $x = 26\%$  and (c)  $x = 35\%$  [(010) orientation], (d)  $x = 17\%$ , and (e)  $x = 48\%$  [( $\bar{2}01$ ) orientation]. For (010) and ( $\bar{2}01$ ) orientations, the HAADF-STEM images were taken from the  $[001]_m$  and  $[010]_m$  zone axis, respectively.

**Figure 5** Fitted Ga 3s and Al 2p core level spectra from (a) (010) and (b) ( $\bar{2}01$ ) oriented  $\beta$ -( $\text{Al}_x\text{Ga}_{1-x}$ ) $_2\text{O}_3$  layers [sample structure (ii)] with different Al compositions after applying the Shirley background subtraction. The Al compositions are determined by comparing the areas of Ga 3s and Al 2p core level peaks.

**Figure 6** (a) O 1s core level spectra of  $(\bar{2}01)$  oriented  $\beta-(\text{Al}_x\text{Ga}_{1-x})_2\text{O}_3$  film for Al composition  $x = 48\%$  with the peak position located at 530.19 eV binding energy. The inset shows the zoomed view of the inelastic background region marked by the black dashed rectangle in O 1s spectra. The bandgap of  $5.79 \pm 0.12$  eV is calculated from the binding energy difference between the O 1s core-level position and the onset of the inelastic background. (b) The bandgaps of  $\beta-(\text{Al}_x\text{Ga}_{1-x})_2\text{O}_3$  films grown on (010),  $(\bar{2}01)$  and (100) oriented  $\beta\text{-Ga}_2\text{O}_3$  substrates as a function of Al compositions, showing good agreement with theoretically predicted bandgap values.

**Figure 7** Schematic energy band diagram of  $\beta-(\text{Al}_x\text{Ga}_{1-x})_2\text{O}_3/\beta\text{-Ga}_2\text{O}_3$  interface, showing the parameters used for determining the valance and the conduction band offsets.

**Figure 8** Fitted Ga  $2p_{3/2}$  and Al 2p core-levels and the valence band (VB) spectra from (010) oriented (a)  $\beta\text{-Ga}_2\text{O}_3$  film [sample structure (i)], (b)  $\beta-(\text{Al}_x\text{Ga}_{1-x})_2\text{O}_3$  film [sample structure (ii)], and (c)  $\beta-(\text{Al}_x\text{Ga}_{1-x})_2\text{O}_3/\beta\text{-Ga}_2\text{O}_3$  heterointerface [sample structure (iii)] with  $x = 0.35$ . Experimental data points are shown as blue open circles and the fitted curves and lines are represented as black dashed lines (for Ga  $2p_{3/2}$  and Al 2p core-levels) and red solid straight lines (for VB spectra), respectively.

**Figure 9** Summary of the valance and conduction band offsets at (a) (010)  $\beta-(\text{Al}_x\text{Ga}_{1-x})_2\text{O}_3/\beta\text{-Ga}_2\text{O}_3$  interfaces for  $x = 16\%$ , 26% and 35%, (b)  $(\bar{2}01)$   $\beta-(\text{Al}_x\text{Ga}_{1-x})_2\text{O}_3/\beta\text{-Ga}_2\text{O}_3$  interfaces for  $x = 17\%$  and 48%. The valance and conduction band offsets with corresponding bandgap energies are represented in blue, red and green, respectively.

**Figure 10** The conduction band offsets ( $\Delta E_c$ ) at (010),  $(\bar{2}01)$  and (100)  $\beta-(\text{Al}_x\text{Ga}_{1-x})_2\text{O}_3/\beta\text{-Ga}_2\text{O}_3$  heterointerfaces as a function of Al compositions. The black, red and blue solid symbols represent the  $\Delta E_c$  for (100), (010) and  $(\bar{2}01)$  orientations, respectively. The solid lines represent the quadratic fitting of the experimentally measured  $\Delta E_c$  values for different orientations,

showing highly orientation-dependent conduction band offsets at  $\beta\text{-(Al}_x\text{Ga}_{1-x})_2\text{O}_3/\beta\text{-Ga}_2\text{O}_3$  heterointerfaces.

Figure 1

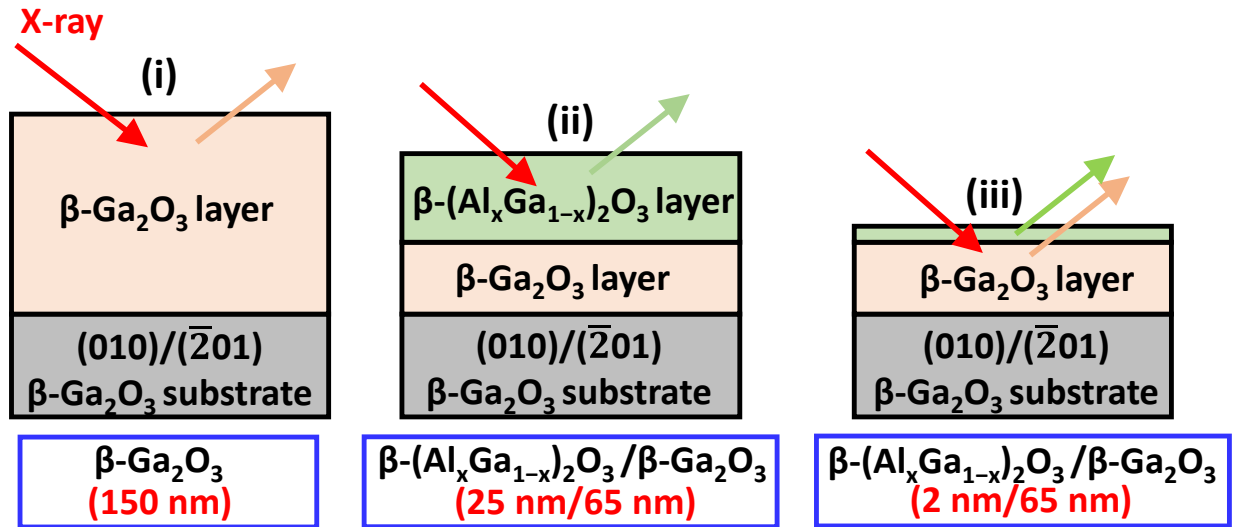


Figure 2

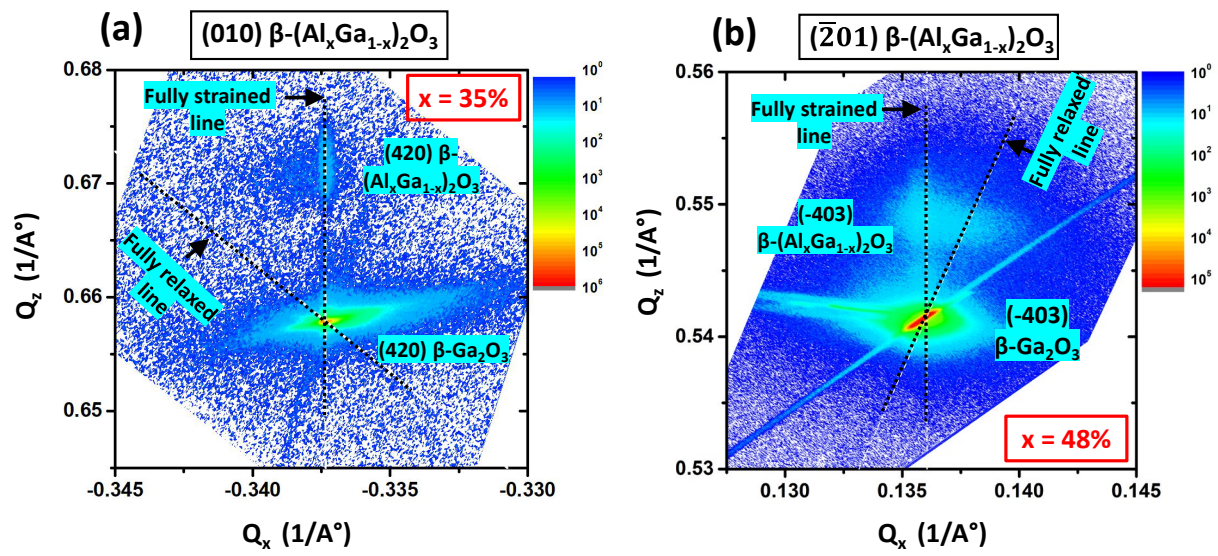


Figure 3

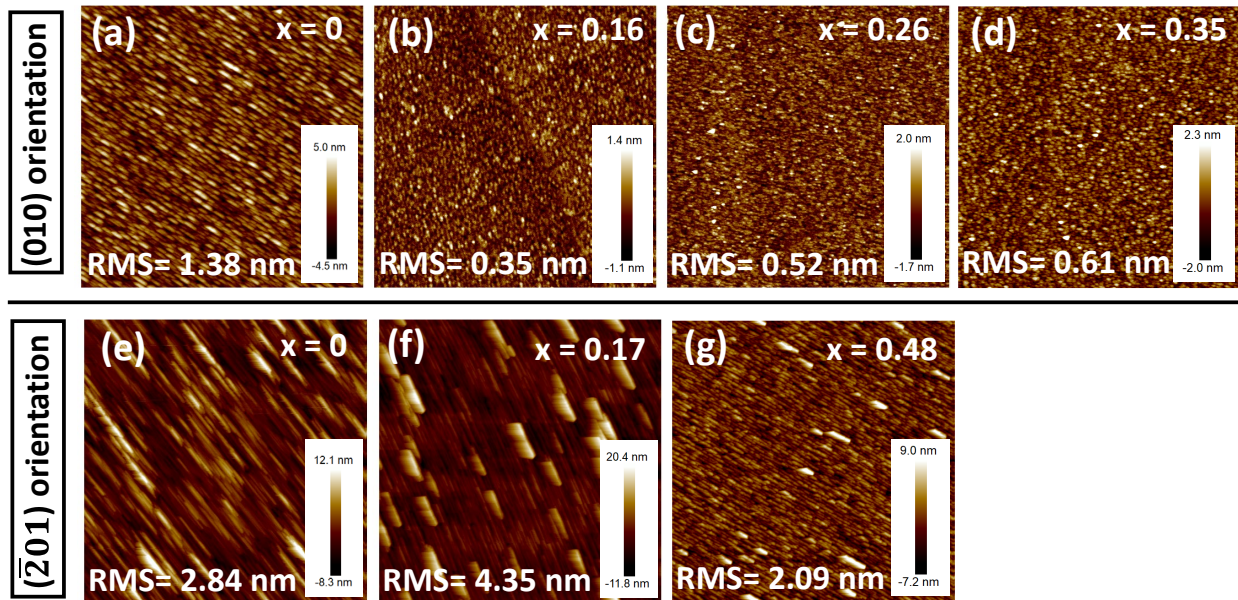


Figure 4

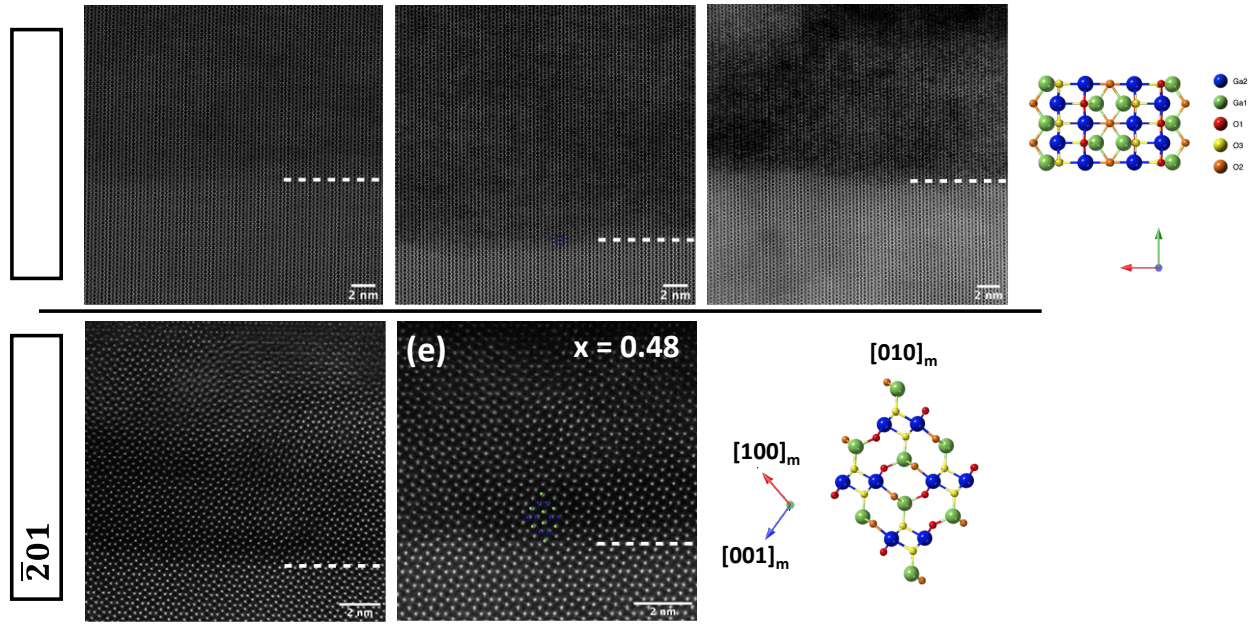


Figure 5

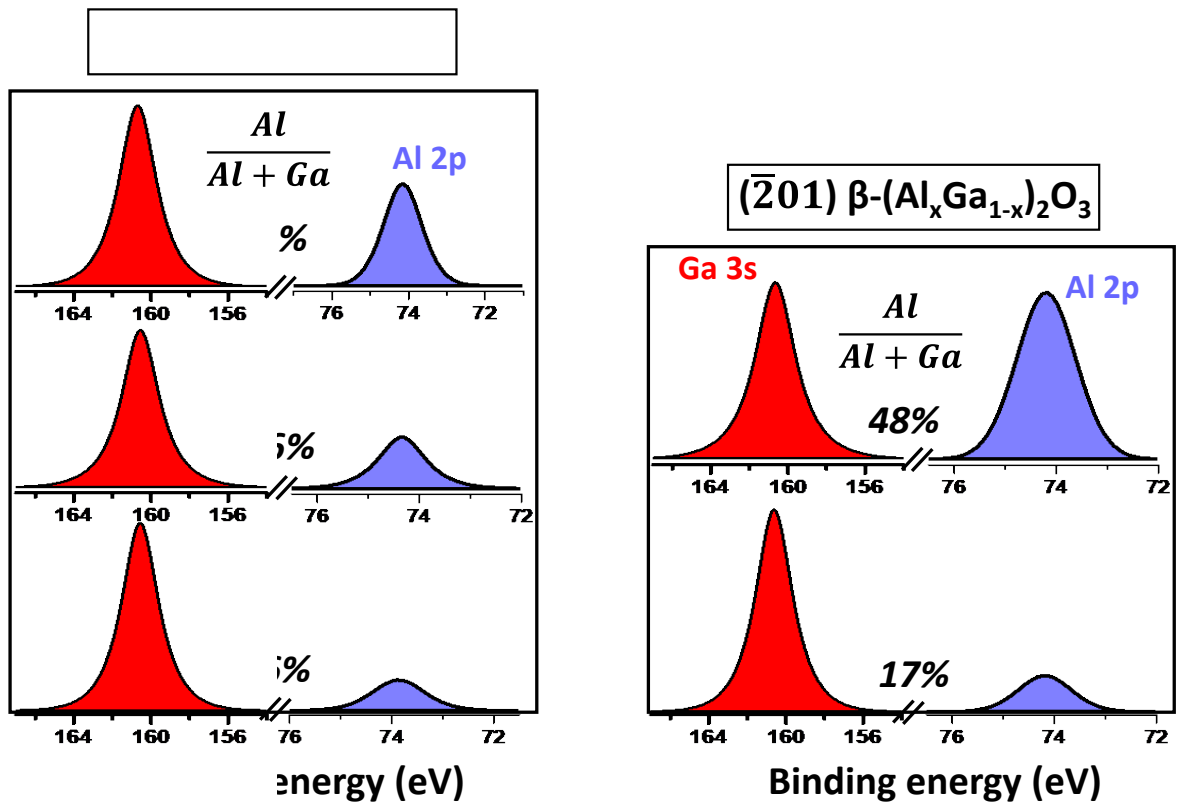


Figure 6

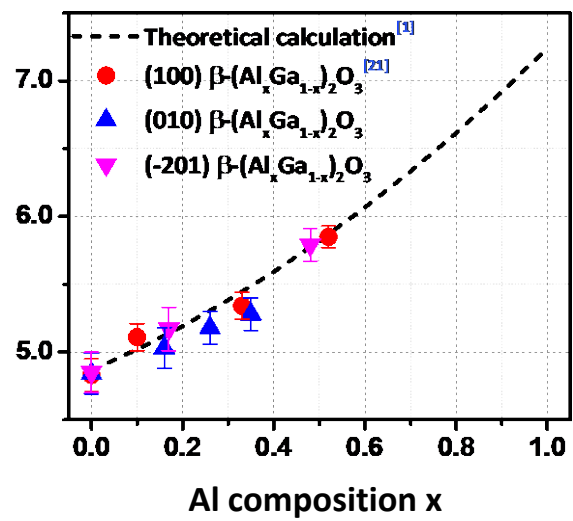
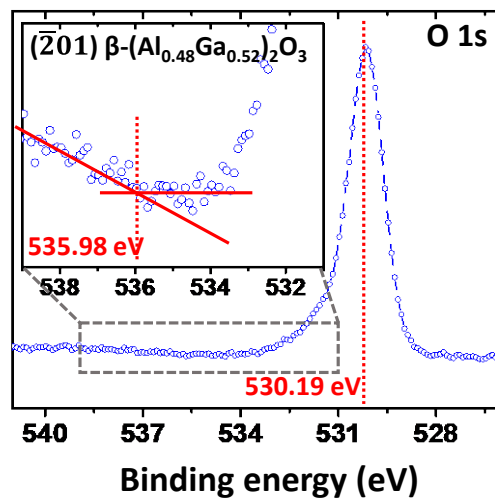


Figure 7

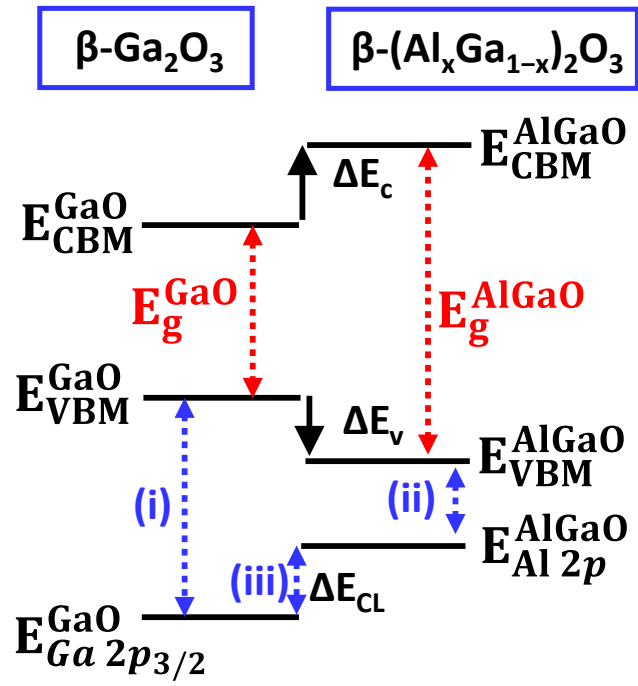


Figure 8

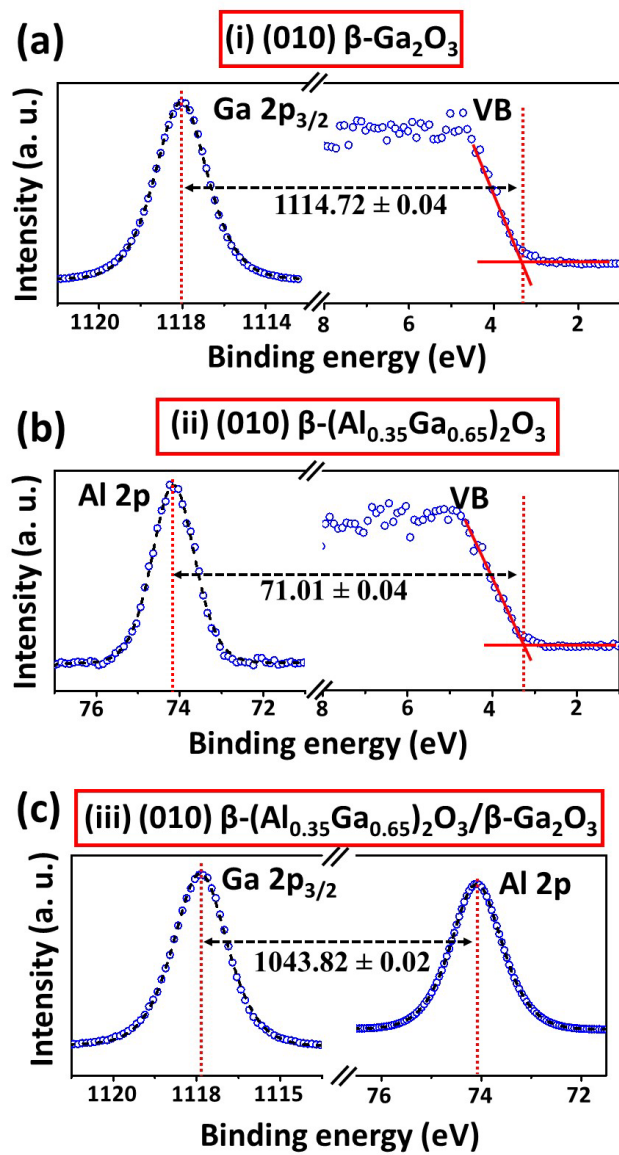


Figure 9

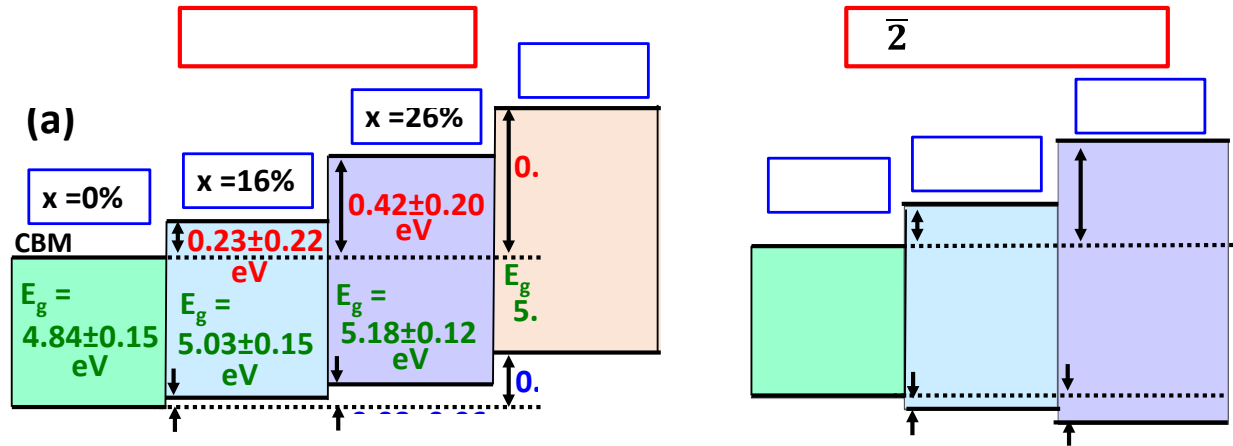


Figure 10

